

AperTO - Archivio Istituzionale Open Access dell'Università di Torino

## Comparison of two depth-averaged numerical models for debris flow runout estimation

### **This is the author's manuscript**

*Original Citation:*

*Availability:*

This version is available <http://hdl.handle.net/2318/1684374> since 2019-03-18T11:08:53Z

*Published version:*

DOI:10.1139/cgj-2017-0455

*Terms of use:*

Open Access

Anyone can freely access the full text of works made available as "Open Access". Works made available under a Creative Commons license can be used according to the terms and conditions of said license. Use of all other works requires consent of the right holder (author or publisher) if not exempted from copyright protection by the applicable law.

(Article begins on next page)

1 **Comparison of two depth averaged numerical models for debris**  
2 **flow runout estimation**

3

4 Vagnon Federico\*

5 Department of Earth Science, University of Torino, Via Valperga Caluso 35, 10125, Turin,  
6 Italy.

7 \*Corresponding author: fvagnon@unito.it, Tel: +39 0116705325

8

9 Pirulli Marina

10 Department of Structural, Geotechnical and Building Engineering, Politecnico di Torino,  
11 Corso Duca degli Abruzzi 24, 10129 Turin, Italy

12 marina.pirulli@polito.it

13

14 Yague Angel

15 Department of Applied Mathematics and Computer Science, ETSI Caminos, Canales y  
16 Puertos, Universidad Politécnica de Madrid (UPM), Madrid, Spain

17 angel.yague@upm.es

18

19 Pastor Manuel

20 Department of Applied Mathematics and Computer Science, ETSI Caminos, Canales y  
21 Puertos, Universidad Politécnica de Madrid (UPM), Madrid, Spain

22 manuel.pastor@upm.es

23 **Abstract**

24 This paper analyses an important aspect of the continuum numerical modeling of rapid  
25 landslides as debris flows: by using the same rheological parameter values, are the results,  
26 obtained with codes that implement the same constitutive equations but a different  
27 numerical solver, equal? In order to answer this question, the two numerical codes  
28 RASH3D and GeoFlow\_SPH are here used to back-analyze the debris flow event occurred  
29 in the Nora stream (Northwestern Italian Alps) in October 2000. Comparison of results  
30 evidenced that the RASH3D best fit rheological values for the Nora event back analysis  
31 overestimated both the final depositional heights and the simulated flow velocities if used  
32 in GeoFlow\_SPH. In order to obtain thickness values comparable with those measured in  
33 situ, it was necessary to re-calibrate GeoFlow\_SPH rheological parameter values. In this  
34 way, with the exception of a larger lateral spreading of the sliding mass given by  
35 RASH3D, both thickness and velocity values were similar for the two numerical codes.

36

37 **Keywords**

38 Debris flow; runout estimation; RASH3D code; GeoFlow\_SPH code; continuum numerical  
39 modelling

## 40 **1. Introduction**

41 Every year thousands of landslides all over the world cause loss of human lives and  
42 enormous economical damages. These phenomena remember us of our society's  
43 vulnerability to natural disasters (Jakob and Hungr 2005).

44 In the last decades, the climate changes have increased the probability of occurrence of a  
45 particular type of landslide: the debris flow. Glacier melting, permafrost degradation,  
46 increase of extreme (short and intense) rainfall are triggering factors for this dangerous  
47 and destructive phenomenon. The main characteristics of debris flows are their  
48 unpredictability, their high velocity and their long travel distances.

49 Since their potential for destruction usually cannot practically be reduced by stabilization  
50 of the source area (Hungr 1995), engineering risk analyses are required, including  
51 prediction of runout parameters (maximum travel distance reached, flow velocities,  
52 thickness and distribution of the deposit). Since it is very difficult to obtain data from  
53 monitoring of real events and to apply statistical methods, others methodologies for  
54 evaluating flow characteristics are required. Numerical models represent a useful tool for  
55 investigating, within realistic geological contexts, the dynamics of these events.

56 Existing models can be divided into two main groups: those that follow empirical  
57 approaches and those that are based on dynamic numerical models (continuum or  
58 discontinuum). Empirical models, based on correlation among historical data (e.g. Cannon  
59 1993, Corominas 1996, Rickenmann 1999), are more practical and easy to use but they  
60 should only be applied to conditions similar to those on which their development are based  
61 (Rickenmann 2005).

62 Alternatively, dynamic numerical models are viable tools for forecasting flow parameters  
63 (e.g. Savage and Hutter 1989, O'Brien et al. 1993, Hungr 1995, Iverson and Delinger  
64 2001, Mc-Dougall and Hungr 2004, Pirulli 2005, Pastor et al. 2009). In particular, the  
65 basic concept of continuum-based methods is that the release mass dynamics can be

66 described in terms of flow-like behaviour. The moving mass can entrain additional  
67 material from the path and eventually deposits, when it reaches slopes that are sufficiently  
68 flat. Whatever code is used, the choice of the rheological law, the terrain characteristics  
69 and the presence of erosion/deposition areas affect the results (Pirulli and Marco, 2010).  
70 Consequently, these methods require an accurate calibration of parameters on the basis of  
71 back analysis of real events for assessing and forecasting potential dangerous areas.  
72 Another important issue is the choice of the most suitable simulation code: Pirulli and  
73 Sorbino (2008) stated that the use of more than one code for simulating debris flow events  
74 is recommended in order to compare runout results, providing and highlighting the main  
75 differences. This aspect is particularly important because it helps users in the decisional  
76 process for assessing potential risks and evaluating/designing possible countermeasures.  
77 The purpose of this paper is to investigate if codes that implement the same governing  
78 equations, but with fundamentally different numerical solvers, produce different results,  
79 when the same rheological law and rheological values are used to model a given case, and  
80 the extent to which obtained results may differ. This is an important aspect and it should  
81 be taken into account by the engineers (e.g. in the design of structural countermeasures  
82 and mapping of dangerous areas). Since one of the main functions of the numerical codes  
83 should be to forecast future events and to predict their effects, their choice becomes, for  
84 the engineers, an important aspect to take into account (Vagnon 2017).  
85 In the following sections the two different continuum-based codes RASH3D (Pirulli 2005)  
86 and GeoFlow\_SPH (Pastor et al. 2009, 2015) are briefly described and used to back-  
87 analyze a real debris flow event occurred in Northern Italy. The obtained results are  
88 compared and discussed.

89

## 90 **2. Continuum mechanics modeling**

91 To apply continuum mechanics to flow-like landslide modeling implies that both  
92 characteristic thickness (H) and length (L) of the flowing mass are assumed to exceed the  
93 size of single moving particles of several times. With this hypothesis, the real moving  
94 mixture, composed of solid and fluid phases, can be replaced by an “equivalent fluid”,  
95 whose properties have to approximate the bulk behaviour of the real mixture.

96 Furthermore, a kinematic boundary condition is imposed on free and bed surfaces  
97 according to which the mass neither enters nor leaves at these two surfaces unless an  
98 erosion law is introduced.

99 Under the above conditions and assuming that the sliding mass is described as a single-  
100 phase, incompressible and homogeneous material (Savage and Hutter 1989, Hungr 1995,  
101 Iverson and Delinger 2001), the motion can be described using the balance of mass and  
102 momentum equations:

$$103 \quad \nabla \cdot v = 0 \quad (1)$$

$$104 \quad \rho \left( \frac{\partial v}{\partial t} + v \cdot \nabla v \right) = -\nabla \cdot \sigma + \rho g \quad (2)$$

105 where  $v = (v_x, v_y, v_z)$  denotes the three-dimensional velocity vector inside the mass in a (x,  
106 y, z) coordinate system that will be discussed later,  $\sigma(x, y, z, t)$  is the Cauchy stress  
107 tensor,  $\rho$  is the mass density and  $g$  is the vector of gravitational acceleration.

108 Depth averaging of these equations and shallow flow assumption require the choice of an  
109 appropriate coordinate system. During the flow, the characteristic thickness (H) of the  
110 flow is considerably smaller than its extent parallel to the bed (L). In the case of  
111 significant slopes, the shallow flow assumption is more significant in a reference frame  
112 linked to the topography and the classical shallow water approximation relating horizontal  
113 and vertical direction is not appropriate (Mangeney-Castelnau et al. 2003). As in the work  
114 by Denlinger and Iverson (2001), the equations are here written in term of a local,

115 orthogonal Cartesian coordinate system in which the z coordinate is normal to the local  
 116 topography.

117 In the reference frame linked to the topography, equations of mass and momentum in the x  
 118 and y direction derived by integration of Navier-Stokes equations (1)-(2) read

$$119 \quad \begin{cases} \frac{\partial h}{\partial t} + \frac{\partial(\bar{v}_x h)}{\partial x} + \frac{\partial(\bar{v}_y h)}{\partial y} = 0 \\ \rho \left( \frac{\partial(\bar{v}_x h)}{\partial t} + \frac{\partial(\bar{v}_x^2 h)}{\partial x} + \frac{\partial(\bar{v}_x \bar{v}_y h)}{\partial y} \right) = \mp \frac{\partial(\bar{\sigma}_{xx} h)}{\partial x} + \frac{\partial(\bar{\sigma}_{xy} h)}{\partial y} + T_{x(z=b)} + \rho g_x h \\ \rho \left( \frac{\partial(\bar{v}_y h)}{\partial t} + \frac{\partial(\bar{v}_y \bar{v}_x h)}{\partial x} + \frac{\partial(\bar{v}_y^2 h)}{\partial y} \right) = + \frac{\partial(\bar{\sigma}_{xy} h)}{\partial x} \mp \frac{\partial(\bar{\sigma}_{yy} h)}{\partial y} + T_{y(z=b)} + \rho g_y h \end{cases} \quad (3)$$

120 where  $\bar{v} = (\bar{v}_x, \bar{v}_y)$  denotes the depth-averaged flow velocity,  $h$  is the flow depth,  $T_x$  and  $T_y$   
 121 are the traction vector components in the x and y directions and  $g_x, g_y$  are the projections  
 122 of the gravity vector along the x and y directions, respectively. The traction vector  $T =$   
 123  $(T_x, T_y, T_z) = -\sigma \cdot n_b$ , where  $n_b$  is the unit vector normal to the bed, read

$$T = \begin{pmatrix} \sigma_{xx} \frac{\partial b}{\partial x} + \sigma_{xy} \frac{\partial b}{\partial y} - \sigma_{xz} \\ \sigma_{xy} \frac{\partial b}{\partial x} + \sigma_{yy} \frac{\partial b}{\partial y} - \sigma_{yz} \\ \sigma_{xz} \frac{\partial b}{\partial x} + \sigma_{yz} \frac{\partial b}{\partial y} - \sigma_{zz} \end{pmatrix}_b$$

124 A scale analysis with respect to  $H/L$  (Gray et al. 1999, Mangeney-Castelnau et al. 2003)  
 125 leads to neglect the acceleration normal to the topography and the horizontal gradients of  
 126 the stresses in the z equation, leading to  $\sigma_{zz} = \rho g_z(h-z)$ . The normal traction reduced to  $T_z$   
 127  $= -\sigma_{zz|_b}$  and  $(\partial/\partial x_i)(h\bar{\sigma}_{xy})$  can be neglected in the z and y depth-averaged momentum  
 128 equations.

129 Depth-average integration simplifies the three-dimensional description of the flow but the  
 130 vertical velocity distribution is lost and replaced with a single average velocity value in  
 131 the flow depth for each point of the flowing mass. Furthermore, the rheological  
 132 characteristics are included in a single term acting at the interface between flow and  
 133 terrain surface.

134 In 1989 depth-averaged equations were applied for the first time to the analysis of  
135 propagation of a granular mass by Savage and Hutter; since then, many numerical models  
136 were progressively implemented. Even if based on the same balance equations and the  
137 same simplifying hypotheses, the above codes mainly differ for the adopted numerical  
138 solver.

139 In the following sections, the characteristics and peculiarity of the two continuum  
140 numerical codes, RASH3D (Pirulli 2005) and GeoFlow\_SPH (Pastor et al. 2009, 2015),  
141 are presented, focusing on both similarities and main differences.

142

### 143 **3. RASH3D versus GeoFlow\_SPH**

144 In continuum dynamics, the equations of motion can be formulated in one of two frames  
145 of reference: Eulerian or Lagrangian. A Eulerian reference frame is fixed in space, while  
146 a Lagrangian reference frame moves with the flow. Furthermore, to perform the mass  
147 balance calculation, a discretisation of the equations has to be made by using a mesh  
148 (structured or unstructured) or a meshless approach. In a meshless scheme, in lieu of a  
149 mesh, balance is determined from the spatial distribution of a number of moving reference  
150 masses (known as particles). The RASH3D and GeoFlow\_SPH codes adopt the first and  
151 the second discretization-approach, respectively. In particular, RASH3D discretizes the  
152 terrain on a general triangular grid with a finite element data structure and it computes the  
153 flow in the different flow directions using a particular control volume; whereas, in  
154 GeoFlow\_SPH, the sliding soil is schematized as a series of nodes with fictitious moving  
155 mass and pressure terms. That is, RASH3D uses a Eulerian method and a fixed reference  
156 system for evaluating flow motion characteristics (for each node of the mesh, velocity and  
157 thickness and their evolution in time are calculated). On the other hand, GeoFlow\_SPH  
158 uses a meshless Lagrangian method known as Smoothed Particle Hydrodynamics (SPH)  
159 and the reference system is integral with the particle position.

160 Both these codes are based on a depth-average continuum mechanics based approach and  
161 they need as input data to run an analysis: i) the pre-event digital elevation model (DEM),  
162 ii) the position and the magnitude of a source area, iii) the rheological law.

163 A relation deduced from the mechanical behaviour of the material has to be imposed  
164 between the tangential stress  $T_t = (T_x, T_y)$  and  $v$  and  $h$  in order to close equations (3). The  
165 depth-averaged mass is then considered as an effective material submitted to an empirical  
166 friction introduced in the tangential traction term  $T_t$  (Pouliquen 1999).

167 Considering a Coulomb-type friction law, the norm of the tangential traction  $\|T_t\|$  at the  
168 bed is related to the norm of the normal traction  $\|T_n\| = |T_z| = |\sigma_{zz}|_b$  at the bed, through a  
169 friction coefficient  $\mu$ , that is  $\|T_t\| \leq \sigma_c = \mu\|T_n\| = \mu\rho g_z h$  and acting opposite to the  
170 velocity (i.e.  $T_i = -\mu\rho g_z h \frac{\bar{v}_i}{\|\bar{v}\|}$ ). The value of  $\sigma_c$  defines the upper bound of the admissible  
171 stresses.

172 Similarly, the Voellmy rheology gives:

$$173 \quad T_i = -\left(\rho g_z h \mu + \frac{\rho g \bar{v}_i^2}{\xi}\right) \frac{\bar{v}_i}{\|\bar{v}\|} \quad i = (x, y) \quad (4)$$

174 where  $\mu$  is the frictional coefficient equals to the tangent of the bulk basal friction angle  
175 and  $\xi$  is the turbulent coefficient.

176 The Voellmy rheology, as stated by many Authors (e.g. Hungr and Evans 1996,  
177 Rickenmann and Koch 1997, Revellino et al. 2004, Pirulli 2009), produces most consistent  
178 results in terms of debris spreading and distribution as well as velocity data when debris  
179 flows are analysed. This is why it has been selected for comparing the two codes results in  
180 the case of Rio Nora debris flow event.

181 It is finally underlined that the two selected codes have been widely validated through the  
182 back analysis of laboratory experiments (e.g. Manzella et al. 2008, Pisani et al. 2013,  
183 Sauthier et al. 2015) and of real events (e.g. Pirulli 2009, Pirulli and Marco 2010, Pirulli  
184 and Pastor 2012, Cascini et al. 2014, Cuomo et al. 2014, Pastor et al. 2014, Pirulli 2016,

185 Dutto et al. 2017, Pirulli et al. 2017), and in the frame of a common benchmark exercise  
 186 (see Pastor et al. 2007, Pirulli and Scavia 2007).

187

### 188 3.1. The RASH3D code

189 The RASH3D code, developed by Pirulli (2005) is an upgrade for modelling landslide run  
 190 out problems of a pre-existing numerical code (SHWCIN) developed by Audusse et al.  
 191 (2000) using a finite volume method.

192 This type of method requires the formulation of the equations in terms of conservation  
 193 laws.

194 The system of equations (3), approximated in accordance with the scale analysis described  
 195 in “Continuum mechanics modelling” section, can be written as

$$196 \frac{\partial U}{\partial t} + \text{div}F(U) = B(U) \quad (5)$$

$$197 \text{ with } U = \begin{pmatrix} h \\ hv_x \\ hv_y \end{pmatrix}, F(U) = \begin{pmatrix} hv_x & hv_y \\ hv_x^2 + \frac{g_z h^2}{2} & hv_x v_y \\ hv_x v_y & hv_y^2 + \frac{g_z h^2}{2} \end{pmatrix} \text{ and } B(U) = \begin{pmatrix} 0 \\ g_x h + \frac{1}{\rho} T_x \\ g_y h + \frac{1}{\rho} T_y \end{pmatrix}$$

198 The system of equations is then discretized on an unstructured triangular mesh with a  
 199 finite element data structure using a particular control volume, which is the median dual  
 200 cell (Pirulli 2005). Dual cells  $C_i$  are obtained by joining the centres of mass of the  
 201 triangles surrounding each vertex  $P_i$  of the mesh (Figure 1).

202 For each point  $P_i$  of the mesh the code gives as output the values in time of flow height,  
 203 velocity in x and y directions and the maximum values of height and velocity reached  
 204 during whole process up to final deposition of the mass.

205

206 **Figure 1.** Triangular finite-element mesh for dual cell  $C_i$  (adapted from Mangeney-  
 207 Castelnau et al. 2003).  $n_{ij}$  normal vector to  $\Gamma_{ij}$  directed from  $P_i$  to  $P_j$ , one of the mesh  
 208 vertexes that surround  $P_i$ ,  $\Gamma_{ij}$ , boundary of the dual cell  $C_i$  separating  $P_i$  from  $P_j$ .

209

210 Under these hypotheses, the finite volume scheme writes as:

$$211 \quad U_i^{n+1} = U_i^n - \sum_{j \in K_i} \frac{\Delta t L_{ij}}{|C_i|} F(U_i^n, U_j^n, n_{ij}) + \Delta t B(U_i^n) \quad (6)$$

212 where  $U_i^{n+1}$ ,  $U_i^n$  is the approximation of the cell average of the exact solution  $U$  for the  $i$ th  
213 cell, at times  $t^n$  and  $t^{n+1}$ , respectively, and  $K_i$  is the set of nodes  $P_j$  surrounding  $P_i$ .  $F(U_i^n,$   
214  $U_j^n, n_{ij})$  denotes an interpolation of the normal component of the flux  $F(U) \cdot n_{ij}$  along  
215 boundary edge  $\Gamma_{ij}$ , with length  $L_{ij}$ , which separates cells  $C_i$  and  $C_j$  (Figure 1),  $\Delta t$  is the  
216 time step,  $|C_i|$  is the area of  $C_i$ ,  $B(U_i^n)$  is the approximation of the  $i$ th cell average of the  
217 exact source term,  $B(U)$ , at time  $t^n$  (Audusse et al. 2000). The summation sign in the  
218 second term of the right hand side of equation (6) indicates that the computation here  
219 includes all the boundary edges of the considered  $i$ th cell. In RASH3D, a proper  
220 calculation of the projection of the term of gravity in equations (3) is obtained, for a finite  
221 volume method and a complex topography, by computing the line of maximum dip of each  
222 cell, projecting it on the plane tangent to the topography and re-projecting the obtained  
223 direction on the  $x$  and  $y$  axes of the reference system (Pirulli, 2005).

224

### 225 **3.2. The GeoFlow\_SPH model**

226 The GeoFlow\_SPH model proposed by Pastor et al. (2009) is based on the theoretical  
227 framework of Hutchinson (1986) and Pastor et al. (2002) and it schematises the  
228 propagating mass as a one-phase mixture of solid particles and water. The governing  
229 equations (3) are solved using the SPH model (Lucy 1977; Gingold and Monaghan 1977).

230 In SPH model, a given function,  $\phi(x)$ , and its spatial derivatives can be approximated by  
231 integral approximations defined in terms of kernel and they can be further approximated  
232 by replacing them with summations over all the corresponding values at the neighbouring  
233 particles in a local domain.

234 The following equality is the starting point of SPH approximation:

$$235 \langle \phi(x) \rangle = \int_{\Omega} \phi(x') W(x' - x, h) dx' \quad (7)$$

236 where  $\langle \phi(x) \rangle$  is the integral approximation of  $\phi(x)$ ,  $\Omega$  is the integration domain,  $W(x'-x, h)$   
237 is the smoothing kernel function and  $h$  is the smoothing length defining the influence area  
238 of  $W$ .

239 The accuracy of the numerical solution and the level of approximation for engineering  
240 purposes are a function of the properties and dimensions of the kernel  $W$ . In particular, the  
241 smoothing kernel function  $W$  has to satisfy three main properties: i) its integration returns  
242 the unity, ii) when  $h$  tends to zero, the kernel function is the Dirac delta function and iii)  
243 when  $|x'-x| > kh$ , with  $k$  a constant that defines the effective area of the smoothing function,  
244  $W$  is equal to 0. The latter condition guaranties that the integration over the entire problem  
245 domain is localized over the support domain of the smoothing function, which coincides  
246 with  $\Omega$ .

247 Equation 7 is valid at continuum level; since, in problem concerning the propagation of  
248 rapid landslide, the information is stored in a discrete framework (e.g. in a series of  
249 nodes), the SPH kernel approximation is converted to discretize forms. Thus, the  
250 propagating mass is discretized through a set of moving ‘particles’ or ‘nodes’ in which  
251 regular distributions are used to approximate the values of functions and derivatives. Each  
252 node,  $i$ , has the following nodal variables:  $h$  is the height of of landslide,  $\bar{v}$  is the depth  
253 averaged velocity,  $T^b$  is the surface vector force at the bottom,  $m$  is a fictitious mass  
254 defined as  $\Omega h$ ,  $\bar{p} = \frac{1}{2} b_3 h^2$  is the averaged pressure term and  $\bar{\sigma}^*$  is the depth averaged  
255 modified stress tensor equals to  $\bar{\sigma} + \bar{p}\delta$ .

256 As consequence, equation 7 can be rewritten as follow:

$$257 \langle \phi(x_i) \rangle = \sum_{j=1}^N \frac{m_j}{\rho_j} \phi(x_j) W_{ij} \quad (8)$$

258 where  $\rho_j$  is the fictitious density of the particle  $j$ ,  $N$  is the number of nodes and  $W_{ij}$  is the  
 259 value of smoothing kernel defined as  $W(x_j-x_i,h)$ . Summarizing, the integral approximation  
 260 of a function  $\phi(x)$  at the node  $i$  is defined as the sum of the function values estimated at  
 261 the nodes  $j$ , included in the support domain  $\Omega$  (Figure 2).

262 Under these hypotheses, the system of equations (3) can be rewritten as:

$$263 \quad \frac{\bar{d}h_i}{dt} = h_i \sum_j \frac{m_j}{h_j} v_{ij} gradW_{ij} \quad (9)$$

$$264 \quad \frac{\bar{d}}{dt} \bar{v}_i = - \sum_j m_j \left( \frac{\bar{p}_i}{h_i^2} + \frac{\bar{p}_j}{h_j^2} \right) gradW_{ij} + \frac{1}{\rho} \sum_j m_j \left( \frac{\bar{\sigma}_i^*}{h_i^2} + \frac{\bar{\sigma}_j^*}{h_j^2} \right) gradW_{ij} + b + \frac{1}{\rho h_i} |N^B| T_i^B \quad (10)$$

265 where  $v_{ij}$  is the difference between  $v_i$  and  $v_j$  and  $|N^B| = \left( \frac{\partial Z^2}{\partial x_1} + \frac{\partial Z^2}{\partial x_2} + 1 \right)^{\frac{1}{2}}$  with  $Z$  the height  
 266 of the basal surface.

267 In GeoFlow\_SPH code, equations (9) and (10) are discretized in time with the explicit  
 268 scheme of fourth order Runge Kutta. As in RASH3D, the terrain information are given by  
 269 DEM; in order to allow searching neighbour particles, an auxiliary temporary structured  
 270 grid, defined by the minimum smoothing length, covering the part of the terrain covered  
 271 by SPH particles is used (Figure 2).

272 The outputs of the code are the values of velocity and depositional height evaluated at  
 273 each time step.

274 A detailed description of the method can be found in Pastor et al. (2015).

275

276 **Figure 2.** Nodes and numerical integration on SPH mesh (Pastor et al. 2009, 2014 and  
 277 2015).

278

### 279 **3.3. Dam break: comparison between numerical and analytical results**

280 This section is devoted to present a benchmark for comparing the predictive capability of  
 281 the two codes. When numerical models are employed, it is fundamental to know the

282 accuracy of numerical results by performing analyses on cases that have analytical  
 283 solutions. This is the case of 1D dam break problem where a vertical wall retaining water  
 284 suddenly collapses (Figure 3). The propagation domain is assumed dry; that is, there is no  
 285 water at the right side of the wall before the collapse. Moreover, no internal and basal  
 286 friction and viscous effects are considered.

287

288 **Figure 3.** 1D dam break problem over a dry bed.

289

290 The initial height condition is given by the piecewise constant function:

$$291 \quad h(x, 0) = \begin{cases} h_L & \text{if } x \leq 0 \\ 0 & \text{if } x > 0 \end{cases} \quad (11)$$

292 and the velocity by:

$$293 \quad u(x, 0) = 0 \quad (12)$$

294 where  $h_L$  is the initial height equals to 10 m.

295 The analytical solutions (Stoker 1957, Guinot 2003) for 1D dam break problem under the  
 296 hypothesis of a dry, frictionless bed are:

$$297 \quad h(x, t) = \begin{cases} h_L & \text{if } x \leq -2\sqrt{gh_L t} \\ \frac{1}{9g} \left( 2\sqrt{gh_L} - \frac{x}{t} \right)^2 & \text{if } -2\sqrt{gh_L t} \leq x \leq 2\sqrt{gh_L t} \\ 0 & \text{if } x \geq 2\sqrt{gh_L t} \end{cases} \quad (11)$$

$$298 \quad u(x, t) = \begin{cases} 0 & \text{if } x \leq -\sqrt{gh_L t} \\ \frac{2}{3} \left( \sqrt{gh_L} + \frac{x}{t} \right) & \text{if } -\sqrt{gh_L t} < x \leq 2\sqrt{gh_L t} \\ 0 & \text{if } x > 2\sqrt{gh_L t} \end{cases} \quad (12)$$

299 Figure 4 shows the comparison between analytical (green dotted line) and numerical  
 300 results obtained with RASH3D (blue line) and Geoflow\_SPH (red line) codes, in terms of  
 301 flow height (Figure 4a) and velocity (Figure 4b) at  $t = 0.5$  s. A good agreement between  
 302 analytical and numerical solutions for each code is found. For what it concerns  
 303 Geoflow\_SPH, its computed solution shows a good approximation of the analytical

304 solution especially in the initiation phase of the flow propagation whereas it overestimates  
305 flow height (and consequently it underestimates the velocity) during the rarefaction phase.  
306 On the contrary, RASH3D solution presents smoother results in the initiation phase (and  
307 consequently it there overestimates the velocity) but a good agreement at the flow front.

308

309 **Figure 4.** Comparison between analytical solution and computed results for flow height  
310 (a) and velocity (b) at  $t = 0.5$  s.

311

### 312 **3.4. Frictional dam break on a slope: comparison between numerical and analytical** 313 **results**

314 In the previous section, the prediction capability of the two codes was evaluated solving  
315 the 1D problem of the collapse of a vertical wall retaining water and comparing the results  
316 with the analytical solution presented by Stoker (1957) and Guinot (2003). Since the two  
317 codes are intended for use with granular material, the case of a frictional fluid behind a  
318 dam on a slope is here considered (Figure 5). Comparing this benchmark with that  
319 presented in section “Dam break: comparison between numerical and analytical results”,  
320 there are two additional terms, originated by the slope and the basal friction.

321

322 **Figure 5.** The frictional dam break problem on an inclined plane.

323

324 The analytical solution used here to validate the RASH3D and GeoFlow\_SPH results was  
325 developed by Mangeney et al. 2000 and it allows to easily calculate the flow height and  
326 depth-averaged flow velocity for a given time ( $t$ ) as follow:

$$327 \quad h(t) = \frac{1}{9g\cos\theta} \left( 2c_0 - \frac{x}{t} + \frac{1}{2}mt \right)^2 \quad (15)$$

$$328 \quad u(t) = \frac{1}{3} \left( 2c_0 + \frac{2x}{t} - mt \right) + mt \quad (16)$$

329 where,  $g$  is the gravity acceleration,  $\theta$  is the slope equals to  $30^\circ$  and the physical quantities  
330  $c_0$  and  $m$  are given by the following equations:

$$331 \quad c_0 = \sqrt{gh_L \cos\theta} \quad (17a)$$

$$332 \quad m = g \cos\theta (\tan\phi - \tan\theta) \quad (17b)$$

333 where  $h_L$  is the initial fluid height and  $\phi$  is the bulk friction angle respectively equal to 10  
334 m and  $25^\circ$ .

335 The equations (15) and (16) are valid outside the region defined by  $x > -c_0 t + 1/2 m t^2$ , where  
336 the fluid height and the velocity are constant and respectively equal to  $h_L$  and  $mt$  and  
337 upstream from the front of the fluid ( $h = 0$  and  $u = mt$ ) defined by  $x > 2c_0 t + 1/2 m t^2$ .

338 In Figure 6, the comparison between analytical (green dotted line) and numerical results  
339 obtained with RASH3D (blue line) and Geoflow\_SPH (red line) codes is shown. As in the  
340 water dam break case, a good agreement between analytical and numerical solutions for  
341 each code was found. For what it concerns flow height, Geoflow\_SPH solution presents  
342 smoother height values in the initiation phase and a moderate overestimation of the front  
343 thickness. RASH3D accentuates the effects of smoothing in the initiation phase but it  
344 shows a negligible overestimation of the front thickness values compared to the analytical  
345 solution.

346 About depth-averaged velocity, it has an opposite trend compared to the height flow: in  
347 fact, where simulated thickness values are smaller than analytical ones, simulated velocity  
348 values are higher and vice-versa. For these reasons, the main differences between  
349 numerical and analytical solutions increase closer to the front flow.

350

351 **Figure 6.** Comparison between analytical solution and computed results for flow height  
352 (a) and velocity (b) at  $t = 30$  s.

353

354 The benchmarks here proposed were used to assess the validity of the discretization  
355 technique presented. Others validation exercises can be found in Pastor et al. 2009, 2014,  
356 2015 and Pirulli 2005.

357

#### 358 **4. Case study: the October 2000 Nora Debris flow**

359 The Nora stream basin (Figure 7), a tributary of the Orco River (Piedmont region,  
360 Northwestern Alps, Italy), was affected in October 2000 by intense rainfall (the average  
361 rainfall value was 400 mm in 60 h, with peak rainfall intensity of 28 mm/h) that caused  
362 the formation of a debris slide (ARPA Piemonte 2003). Due to the steep drainage network,  
363 the intense surface runoff and the altered gneissic bedrock, the debris slide rapidly  
364 transformed into a channelized non-cohesive debris flow (Pirulli and Marco 2010).  
365 Although residual pockets of debris located along the channel were re-mobilized, due to  
366 their smaller volumes than main moving mass, the entrainment of material during runout  
367 can be neglected.

368

369 **Figure 7.** Location of the Nora basin (Orco River valley) in Italy.

370

371 Reaching the fan apex, the debris split into two main branches (Figure 8), one on the  
372 orographic left with thickness values ranging from 0,5 and 1,5 m; the other, on the  
373 orographic right with thickness varying between 0,2 and 0,8 m.

374 After post-event observations (in both the source zone and the depositional areas) and  
375 comparison between ground profile pre- and post-event, the bulk debris volume was  
376 estimated at approximately 10000 m<sup>3</sup>.

377

378 **Figure 8.** Deposition area and debris thickness distribution of the October 2000 Nora  
379 debris flow.

380

## 381 **5. Discussion**

382 Do different numerical codes that implement the same governing equations (3), but with  
383 fundamentally different numerical solvers, give same results or not? Are the differences  
384 relevant? What are the consequences concerning the design of potential structural  
385 countermeasures?

386 In order to answer these questions, in the present section the comparison of results coming  
387 from analyses performed using the two numerical codes presented above are showed.

388 The Nora event was already studied and back analysed with the RASH3D code by Pirulli  
389 and Marco (2010). The best-fit numerical simulation was obtained using a 5m grid spacing  
390 DEM and considering a Voellmy rheology with  $\mu=0,1$  and  $\xi=200$  m/s<sup>2</sup>.

391 Note that in contrast with finite difference methods, where pointwise values are  
392 approximated, and finite element methods, where basis functions are approximated, in a  
393 finite volume method, which is used in RASH3D, the unknowns approximate the average  
394 of the solution over the domain grid cell.

395 Starting from these results, the same analysis, keeping unchanged the rheological  
396 parameter values, was carried out using GeoFlow\_SPH code. As already mentioned, the  
397 meshless particle codes, as GeoFlow\_SPH, do not required fixed grid and all of the  
398 calculations are performed directly at the particle-centred location. Despite this, beside the  
399 5 m topographic mesh (which provides the topography of the problem), GeoFlow\_SPH  
400 requires that a secondary grid is used for the debris flow source area definition. In the Rio  
401 Nora case, the Authors assumed a 1m spacing secondary grid and consequently a source  
402 area made of 212 points was obtained. The smoothing length was set to 2 m.

403 The topographic mesh resolution for RASH3D code and the secondary grid resolution and  
404 dimension of the smoothing length for GeoFlow\_SPH have (considering the same  
405 computational power) a great weight on the computational time. For the Rio Nora case, the

406 computational time of GeoFlow\_SPH code (5m spacing topography grid, 1m spacing  
407 secondary grid) is lower than RASH3D one (5m spacing topography grid), since the  
408 computations are made on a set of arbitrarily distributed particles (secondary mesh), which  
409 are not connected with fixed grid (topography mesh). In particular, using the same  
410 workstation, GeoFlow\_SPH computation time is less than 20 times with respect to  
411 RASH3D.

412 In Figure 9, significant differences can be observed between GeoFlow\_SPH and RASH3D  
413 simulation especially within the depositional area. In particular:

- 414 - GeoFlow\_SPH overestimates the depositional thickness values with respect to the  
415 RASH3D code. It results a zone located at the orographic left of the deposition area  
416 where the depositional height reaches 2,7 m (the maximum on site measured  
417 depositional height was 1,5 m);
- 418 - GeoFlow\_SPH simulation does not reach a satisfactory approximation of the  
419 depositional area shape.

420

421 **Figure 9.** Comparison between RASH (a) and GeoFlow\_SPH (b) propagation path  
422 (deposition values) at the end of the numerical simulation carried out using Voellmy  
423 rheology with  $\mu=0,1$  and  $\xi=200$  m/s<sup>2</sup>.

424

425 Furthermore, analyzing the flowing path at different time step (Figure 10), it is possible  
426 to notice that:

- 427 - At a given time, the travel distance computed with GeoFlow\_SPH is greater than that  
428 evaluated with RASH3D code. This means that, being equal the rheological parameter  
429 values, the flow simulated in GeoFlow\_SPH is faster;
- 430 - RASH3D simulation evidences a pronounced lateral spreading of the flowing mass.

431

432 **Figure 10.** RASH3D (left) and GeoFlow\_SPH (right) simulation at different time steps  
433 using the same rheological parameters. The two simulations show differences both in term  
434 of velocity (flow simulated using SPH is faster) and shape (RASH3D shows a larger  
435 lateral spreading).

436

437 **Figure 11.** Comparison of the two numerical code results in terms of velocity differences  
438 at time step equal to 50 s (a) and velocity values obtained during whole simulation (b).

439

440 Figure 11 shows the differences between velocity values obtained using GeoFlow\_SPH  
441 and RASH3D at the same time step (a) and the differences between maximum velocity  
442 values reached during the whole simulation (b). Analyzing Figure 11a, the above  
443 observations are confirmed. It is in fact possible to notice that the positive variation of  
444 velocity (dark red color) corresponds to the front of the GeoFlow\_SPH simulated flow; on  
445 the contrary, the negative variation (dark green) marks the lateral spreading of the  
446 RASH3D simulation. Differences between calculated velocities are not appreciable (less  
447 than 5 m/s) within the flow body. Concerning the variation of maximum calculated  
448 velocities (Figure 11b), it is interesting to underline that the most significant differences  
449 are in the upper part of the stream, where the channel is steeper, whereas in  
450 correspondence of the alluvial fan there are only appreciable differences between  
451 evaluated velocity at the boundary of the deposition area.

452 Others simulations were run in order to also find the best-fit between depositional area and  
453 GeoFlow\_SPH results. The best correspondence between depositional height and spatial  
454 distribution of the deposit was obtained with  $\mu=0,08$  and  $\xi=100 \text{ m/s}^2$  (Figure 12).

455

456 **Figure 12.** Back calculated GeoFlow\_SPH final deposit using Voellmy rheology with  
457  $\mu=0,08$  and  $\xi=100 \text{ m/s}^2$ .

458

459 Comparing the numerical results of the two calibrated codes, Figure 13 evidences a good  
460 correspondence between the numerically calculated depositional height and in situ  
461 surveyed deposit thickness distribution. It is possible, in particular to notice that:

- 462 - The shape of the flowing mass is slightly different for the two codes: in RASH3D is  
463 evident a pronounced lateral spreading along the channel. Furthermore, RASH3D  
464 flow shows a greater elongation with respect to GeoFlow\_SPH simulated flowing  
465 mass.
- 466 - In this case GeoFlow\_SPH velocities are slower than those of RASH3D.

467

468 **Figure 13.** Comparison between RASH3D (left) and GeoFlow\_SPH (right) simulation at  
469 different time steps using Voellmy rheology with  $\mu=0,1$  and  $\xi=200 \text{ m/s}^2$  and  $\mu=0,08$  and  
470  $\xi=100 \text{ m/s}^2$  respectively.

471

472 **Figure 14.** Differences between maximum velocity values evaluated during the whole  
473 simulation using Geoflow\_SPH and RASH3D best-fit rheological parameters.

474

475 Analyzing the variation of the maximum velocity values computed using the two codes  
476 and their best-fit rheological parameters (Figure 14) it is clear that, along the simulated  
477 flow path, there are no relevant differences especially in the depositional area (velocity  
478 differences vary between -5 and 5 m/s). The most relevant difference is observed along the  
479 boundary of the run out path. RASH3D overestimates the lateral spreading of the flow  
480 with respect to GeoFlow\_SPH. This aspect also emerges in the most compact  
481 configuration of the GeoFlow\_SPH deposit with respect to RASH3D.

482 The fact that the rheological parameter values are not interchangeable, from an  
483 engineering point of view, has relevant consequences. For instance, hypothesizing the

484 construction of a protection structure at the apex point of the alluvial fan (cfr, Figure 7), it  
485 is evident that numerical GeoFlow\_SPH velocity is about 10% greater than that calculated  
486 using RASH3D best-fit rheological values (Table 1). Instead, there are no differences  
487 between the values of maximum flow height.

488

489 **Table 1.** Comparison between numerical results at the apex of alluvial fan calculated  
490 using RASH3D and GeoFlow\_SPH with the same rheology (Voellmy with  $\mu=0,1$  and  
491  $\xi=200 \text{ m/s}^2$ ).

492

## 493 **6. Conclusions**

494 The two codes RASH3D and GeoFlow\_SPH, based on a continuum mechanics approach,  
495 were used to back-analyze the debris flow event occurred in October 2000 at the Nora  
496 Basin, Northwestern Italian Alps.

497 The presented back analysis evidences that both modelling of past debris flow events and  
498 forecasting of future scenarios require to understand and quantify the result discrepancy  
499 generated by the use of different numerical codes. The analyses carried out in this paper  
500 clearly show that, even if a rheology is selected to back-analyze the same case study with  
501 different codes, the obtained calibrated values of rheological parameters are not  
502 interchangeable among the codes. This fact has important consequences in the definition  
503 of risk scenarios or for planning debris flow countermeasures.

504 Summarizing, the uncertainties related to evaluation of propagation characteristics are  
505 consequences of both choice of the numerical code and rheological parameter values. This  
506 is a key point that has to be taken into account by practicing engineers that use codes  
507 rather than produce them.

508 Concerning the analyzed case, it emerges that:

- 509 - Adopting the same rheological parameter values the two codes give different areal  
510 depositional distribution and different velocity and thickness values;
- 511 - RASH3D code always gives a larger lateral mass spreading with respect to  
512 GeoFlow\_SPH;
- 513 - In order to obtain comparable results in terms of depositional height distribution, the  
514 best combination of rheological parameters for GeoFlow\_SPH is  $\mu=0,08$  and  $\xi=100$   
515  $m/s^2$ ;
- 516 - The main differences between the two codes are related to velocity values (the  
517 GeoFlow\_SPH velocity value results 10% greater than the RASH3D ones, by using  
518 RASH3D best fit rheological values). No significant differences between maximum  
519 depth values are emerged.

520

## 521 **References**

522 ARPA Piemonte. 2003. Eventi alluvionali in Piemonte. Evento alluvionale regionale del  
523 13-16 ottobre 2000. Agenzia Regionale per la Protezione Ambientale (ARPA) Piemonte,  
524 Turin, Italy.

525

526 Audusse, E., Bristeau, M.O., Perthame, B. 2000. Kinetic schemes for Saint-Venant  
527 equations with source terms on unstructured grids. Institut National de Recherche en  
528 Informatique et Automatique, LeChesnay, France. Rapport de Recherche, No. 3989, 1-44.

529

530 Cannon, S.H. 1993. An empirical model for the volume-change behaviour of debris flows.  
531 *In* Proceedings of ASCE National Conf. On Hydraulic Engineering, San Francisco,  
532 California, July 25-30, 1768-1773.

533

534 Cascini, L., Cuomo, S., Pastor, M., Sorbino, G. and Piciullo, L. 2014. SPH run-out  
535 modelling of channelised landslides of the flow type. *Geomorphology*, 214, 502–513.  
536

537 Corominas, J. 1996. The angle of reach as a mobility index for small and large  
538 landslides. *Canadian Geotechnical Journal*, **33**(2), 260–271.  
539

540 Cuomo, S., Pastor, M., Cascini, L., and Castorino, G.C. 2014. Interplay of rheology and  
541 entrainment in debris avalanches: a numerical study. *Canadian Geotechnical Journal*  
542 **51**(11): 1318–1330.  
543

544 Dutto, P., Stickle, M.M., Pastor, M., Manzanal, D., Yague, A., Tayyebi, and others. 2017.  
545 Modelling of Fluidised Geomaterials: The Case of the Aberfan and the Gypsum Tailings  
546 Impoundment Flowslides. *Materials*, **10**, 562, 1-21.  
547

548 Gray, J. M. N. T., Wieland, M. and, Hutter, K. 1999. Gravity-driven free surface flow of  
549 granular avalanches over complex basal topography. *Proc. Royal Soc. London. Ser. A*, 455  
550 (1841).  
551

552 Gingold, R. A., and Monaghan, J. J. 1977. Smoothed particle hydrodynamics: theory and  
553 application to non-spherical stars. *Monthly Notices of the Royal Astronomical Society*,  
554 **181**(3), 375–389.  
555

556 Guinot, V. 2003. Godunov-type schemes. An introduction for Engineers. Elsevier,  
557 Amsterdam.  
558

559 Hungr, O. 1995. A model for the runout analysis of rapid flow slides, debris flows, and  
560 avalanches. *Canadian Geotechnical Journal*, **32**(4), 610–623.

561

562 Hungr, O. and Evans, S. G. 1996. Rock avalanche runout prediction using a dynamic  
563 model. *Landslides*, 233–238.

564

565 Hutchinson, J. N. 1986. A sliding–consolidation model for flow slides. *Canadian*  
566 *Geotechnical Journal*, **23**(2), 115–126.

567

568 Iverson, R. M., and Denlinger, R. P. 2001. “Flow of variably fluidized granular masses  
569 across three-dimensional terrain: 1. Coulomb mixture theory.” *Journal of Geophysical*  
570 *Research: Solid Earth*, **106**(B1), 537–552.

571

572 Jakob, M., and Hungr, O. 2005. *Debris-flow hazards and related phenomena*. Springer-  
573 Verlag, Berlin.

574

575 Lucy, L. B. 1977. A numerical approach to the testing of the fission hypothesis. *The*  
576 *Astronomical Journal*, **82**, 1013.

577

578 Mangeney, A., Heinrich, P., Roche, R. 2000. Analytical Solution for Testing Debris  
579 Avalanche Numerical Models. *Pure appl. geophys.* **157**, 1081–1096.

580

581 Mangeney-Castelnau A., Vilotte J.-P., Bristeau M.O., Perthame B., Bouchut F., Simeoni  
582 C., Yernini S. 2003. Numerical modelling of avalanches based on Saint-Venant equations  
583 using a kinetic scheme. *Journal Geophys. Res.* **108** (B11), 1-18.

584

585 Manzella, I., Pirulli, M., Naaim, M., Serratrice, J.F., Labiouse, V. 2008. Numerical  
586 modelling of a rock avalanche laboratory experiment in the framework of the  
587 “Rockslidetec” alpine project. *In* Landslides and Engineered Slopes: Procs. 10th  
588 International Symposium on Landslides and Engineered Slopes. *Edited by* Chen Z. et al.;  
589 Xi’an, Cina, 30 Giugno - 4 Luglio 2008, Taylor & Francis Group, London, Vol. 1, 835-  
590 841.

591

592 Mcdougall, S., and Hungr, O. 2005. Dynamic modelling of entrainment in rapid  
593 landslides. *Canadian Geotechnical Journal*, **42**(5), 1437–1448.

594

595 O'brien, J. S., Julien, P. Y., and Fullerton, W. T. 1993. Two-Dimensional Water Flood and  
596 Mudflow Simulation. *Journal of Hydraulic Engineering*, **119**(2), 244–261.

597

598 Pastor, M., Quecedo, M., Merodo, J. A. F., Herreros, M. I., González, E., and Mira, P.  
599 2002. Modelling tailings dams and mine waste dumps failures. *Géotechnique*, **52**(8), 579–  
600 591.

601

602 Pastor, M., Blanc, T., Pastor, M.J., Sanchez, M., Haddad, B., Mira, P., Fernandez Merodo,  
603 J.A., Herreros, I., and Dremptic, V. 2007. A SPH depth integrated model with pore  
604 pressure coupling for fast landslides and related phenomena. *In* Procs. of the 2007  
605 International Forum on Landslide Disaster Management, *Edited by* K. Ho and V. Li, Hong  
606 Kong, 10-12 December 2007, Vol. II, 987-1014.

607

608 Pastor, M., Haddad, B., Sorbino, G., Cuomo, S., and Dremptic, V. 2009. A depth-  
609 integrated, coupled SPH model for flow-like landslides and related

610 phenomena. *International Journal for Numerical and Analytical Methods in Geomechanics*,  
611 **33**(2), 143–172.

612

613 Pastor, M., Haddad, V., Mira, P., Fernandez-Merodo, J.A. 2014. Depth averaged models  
614 for rock avalanche propagation: an SPH approach. *In Rock Slope Stability 2014*;  
615 Marrakesh, Morocco, 2 - 4 April 2014, 35-58.

616

617 Pastor, M., T. Blanc, B. Haddad, V. Dremptic, Mila Sanchez Morles, P. Dutto, and  
618 others. 2015. Depth Averaged Models for Fast Landslide Propagation: Mathematical,  
619 Rheological and Numerical Aspects. *Archives of Computational Methods in Engineering*.  
620 **22**, 67–104.

621

622 Pirulli, M. 2005. Numerical modelling of landslide runout, a continuum mechanics  
623 approach. Ph.D dissertation, Politecnico of Turin, Turin, Italy.

624

625 Pirulli, M., Scavia, C. 2007. A set of benchmark tests to assess the performance of a  
626 continuum mechanics depth-integrated model. *In Procs. of the 2007 International Forum  
627 on Landslide Disaster Management, Edited by K. Ho and V. Li, Hong Kong, 10-12  
628 December 2007, Vol. II, 1015-1042.*

629

630 Pirulli, M., and Sorbino, G. 2008. Assessing potential debris flow runout: a comparison of  
631 two simulation models. *Natural Hazards and Earth System Science*, **8**(4), 961–971.

632

633 Pirulli, M. 2009. The Thurwieser rock avalanche (Italian Alps): Description and dynamic  
634 analysis. *Engineering Geology*, **109**(1-2), 80–92.

635

636 Pirulli, M., and Marco, F. 2010. Description and numerical modelling of the October 2000  
637 Nora debris flow, Northwestern Italian Alps. *Canadian Geotechnical Journal*, **47**(2), 135–  
638 146.

639

640 Pirulli, M., and Pastor, M. 2012. Numerical study on the entrainment of bed material into  
641 rapid landslides. *Geotechnique*, **62**(11), 959-972.

642

643 Pirulli, M. 2016. Numerical simulation of possible evolution scenarios of the Rosone  
644 deep-seated gravitational slope deformation (Italian Alps, Piedmont). *Rock Mechanics and*  
645 *Rock Engineering*, **49**(6), 2373-2388.

646

647 Pirulli, M., Barbero, M., Marchelli, M., and Scavia, C. 2017. The failure of the Stava  
648 Valley tailings dams (Northern Italy): numerical analysis of the flow dynamics and  
649 rheological properties. *Geoenvironmental Disasters*, **4**(3), 1-15.

650

651 Pisani, G., Pirulli, M., Labiouse, V., and Scavia, C. 2013. Influence of bed curvature on  
652 the numerical modelling of unconstrained granular materials. *In* *Landslide Science and*  
653 *Practice - Volume 3: Spatial Analysis and Modelling; Edited by Margottini, C., Canuti, P.,*  
654 *and Sassa, K.; Springer - Berlin; pp. 271-276.*

655

656 Pouliquen, O. 1999. Scaling laws in granular flows down rough inclined planes. *Physics of*  
657 *fluids*, **11**(3), 542-548.

658

659 Revellino, P., Hungr, O., Guadagno, F. M., and Evans, S. G. 2004. Velocity and runout  
660 simulation of destructive debris flows and debris avalanches in pyroclastic deposits,  
661 Campania region, Italy. *Environmental Geology*, **45**(3), 295–311.

662

663 Rickenmann, D., and Koch, T. 1997. Comparison of debris flow modelling approaches. *In*  
664 *Proceedings of the 1st Int. Conf. On Debris Flow Hazards Mitigation: Mechanics,*  
665 *Prediction and Assessment*, ASCE, Reston, VA, USA, 576-585.

666

667 Rickenmann, D. 1999. Empirical relationships for debris flows. *Natural Hazards*, **19**(1),  
668 47–77.

669

670 Rickenmann, D. 2005. Runout prediction methods. *Debris-flow Hazards and Related*  
671 *Phenomena Springer Praxis Books*, 305–324.

672

673 Sauthier, C., Pirulli, M., Pisani, G., Scavia, C., Labiouse, V. (2015). Numerical modelling  
674 of gravel unconstrained flow experiments with the DAN3D and RASH3D codes.  
675 *Computers & Geosciences*, **85**, 81-90.

676

677 Savage, S. B., and Hutter, K. 1989. The motion of a finite mass of granular material down  
678 a rough incline. *Journal of Fluid Mechanics*, **199**(1), 177.

679

680 Stoker, JJ. 1953. *Water Waves*. Interscience: New York.

681

682 Vagnon, F. 2017. Theoretical and experimental study on the barrier optimization against  
683 debris flow risk. Ph.D dissertation, University of Turin, Turin, Italy.

684

685 **List of symbols**

686  $B(U)$  = source term;

687 DEM = Digital Elevation Model;

688  $\Phi(x)$  = given function;

689  $\langle \Phi(x) \rangle$  = integral approximation of the given function;

690  $F(U)$  = flux term;

691  $g$  = gravitational acceleration;

692  $H$  = characteristic flow thickness;

693  $L$  = characteristic length of flowing mass;

694  $m_i$  = node mass;

695  $n_b$  = unit vector normal to bed;

696  $N$  = number of nodes;

697  $\mu$  = frictional coefficient;

698  $\xi$  = turbulent coefficient;

699  $\bar{p}_t$  = average pressure term;

700  $\rho$  = mass density;

701  $\Omega$  = integration domain;

702 SPH = Smooth Particle Hydrodynamics.

703  $\sigma(x,y,z,t)$  = Cauchy stress tensor;

704  $T(T_x, T_y, T_z)$  = traction vector;

705  $t_{ib}$  = surface vector force at the bottom of the flow;

706  $\tau$  = shear stress;

707  $v = (v_x, v_y, v_z)$  = flow velocity;

708  $\bar{v} = (\bar{v}_x, \bar{v}_y)$  = depth-averaged flow velocity;

709  $U$  = velocity vector;

710  $W$  = kernel of linear function.

711 **Tables**

712 **Table 1.** Comparison between numerical results at the apex of alluvial fan calculated  
713 using RASH3D and GeoFlow\_SPH with the same rheology (Voellmy with  $\mu=0,1$  and  
714  $\xi=200 \text{ m/s}^2$ ).

---

<b>Code</b>	<b>Rheological law</b>	<b>v<sub>max</sub> [m/s]</b>	<b>h<sub>max</sub> [m]</b>
RASH3D	Voellmy: $\mu=0.1 - \xi=200 \text{ m/s}^2$	8,76	2,04
GeoFlow_SPH		9,57	2,05

---

715

716

717 **Figure captions**

718 **Figure 1.** Triangular finite-element mesh for dual cell  $C_i$  (adapted from Mangeney-  
719 Castelnau et al. 2003).  $n_{ij}$  normal vector to  $\Gamma_{ij}$  directed from  $P_i$  to  $P_j$ , one of the mesh  
720 vertexes that surround  $P_i$ ,  $\Gamma_{ij}$ , boundary of the dual cell  $C_i$  separating  $P_i$  from  $P_j$ .

721 **Figure 2.** Nodes and numerical integration on SPH mesh (Pastor et al. 2009)

722 **Figure 3.** 1D dam break problem over a dry bed.

723 **Figure 4.** Comparison between analytical solution and computed results for flow height  
724 (a) and velocity (b) at  $t = 0.5$  s.

725 **Figure 5.** The frictional dam break problem on an inclined plane.

726 **Figure 6.** Comparison between analytical solution and computed results for flow height  
727 (a) and velocity (b) at  $t = 30$  s.

728 **Figure 7.** Location of the Nora basin (Orco River valley) in Italy.

729 **Figure 8.** Deposition area and debris thickness distribution of the October 2000 Nora  
730 debris flow.

731 **Figure 9.** Comparison between RASH (a) and GeoFlow\_SPH (b) propagation path  
732 (deposition values) at the end of the numerical simulation carried out using Voellmy  
733 rheology with  $\mu=0,1$  and  $\xi=200$  m/s<sup>2</sup>.

734 **Figure 10.** RASH3D (left) and GeoFlow\_SPH (right) simulation at different time steps  
735 using the same rheological parameters. The two simulations show differences both in term  
736 of velocity (flow simulated using SPH is faster) and shape (RASH3D shows a larger  
737 lateral spreading).

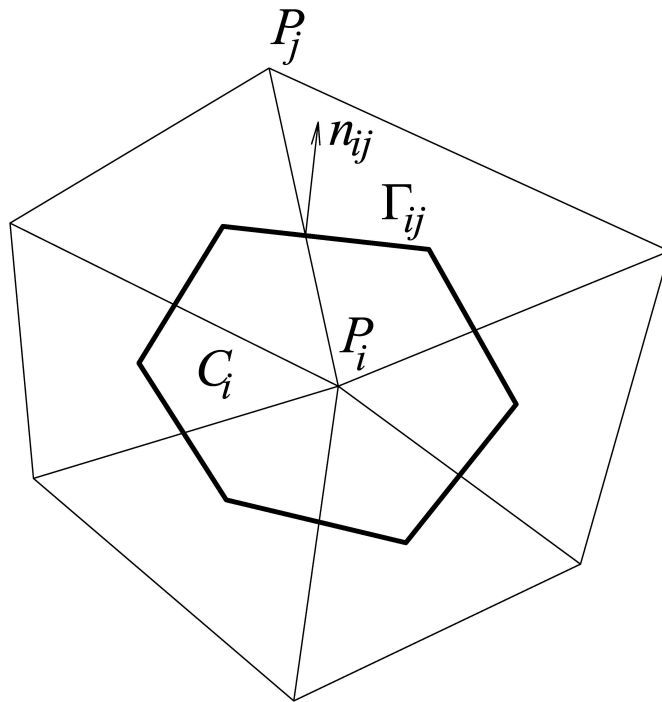
738 **Figure 11.** Comparison of the two numerical code results in terms of velocity differences  
739 at time step equal to 50 s (a) and velocity values obtained during whole simulation (b).

740 **Figure 12.** Back calculated GeoFlow\_SPH final deposit using Voellmy rheology with  
741  $\mu=0,08$  and  $\xi=100$  m/s<sup>2</sup>.

742 **Figure 13.** Comparison between RASH3D (left) and GeoFlow\_SPH (right) simulation at  
743 different time steps using Voellmy rheology with  $\mu=0,1$  and  $\xi=200 \text{ m/s}^2$  and  $\mu=0,08$  and  
744  $\xi=100 \text{ m/s}^2$  respectively.

745 **Figure 14.** Differences between maximum velocity values evaluated during the whole  
746 simulation using Geoflow\_SPH and RASH3D best-fit rheological parameters.

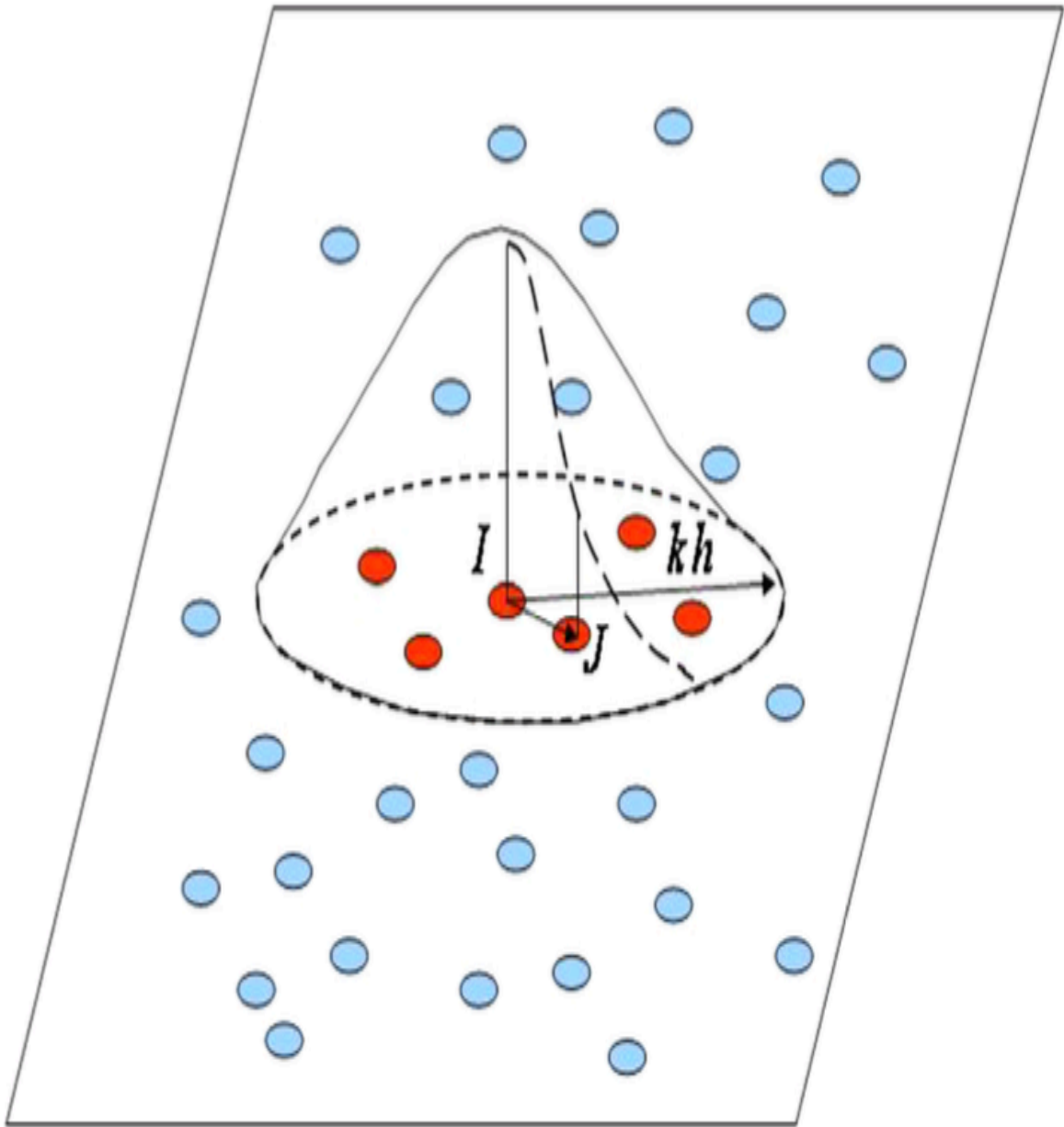
747



749

750 **Figure 1.** Triangular finite-element mesh for dual cell  $C_i$  (adapted from Mangeney-  
751 Castelnau et al. 2003).  $n_{ij}$  normal vector to  $\Gamma_{ij}$  directed from  $P_i$  to  $P_j$ , one of the mesh  
752 vertexes that surround  $P_i$ ,  $\Gamma_{ij}$ , boundary of the dual cell  $C_i$  separating  $P_i$  from  $P_j$ .

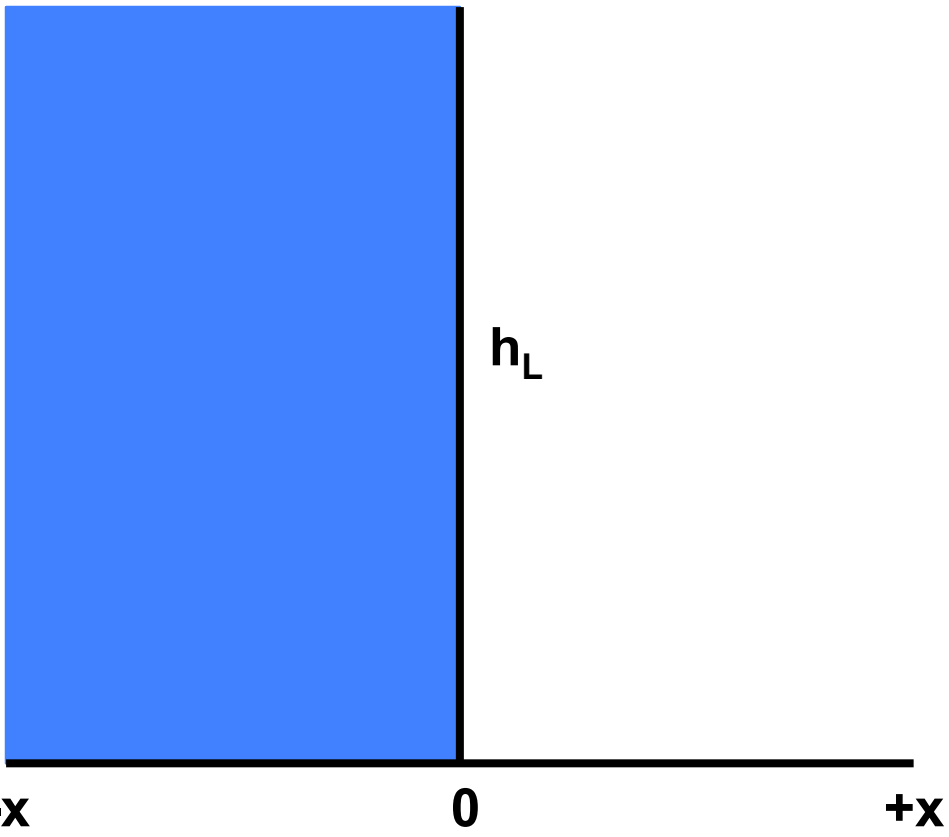
753



754

755 **Figure 2.** Nodes and numerical integration on SPH mesh (Pastor et al. 2009)

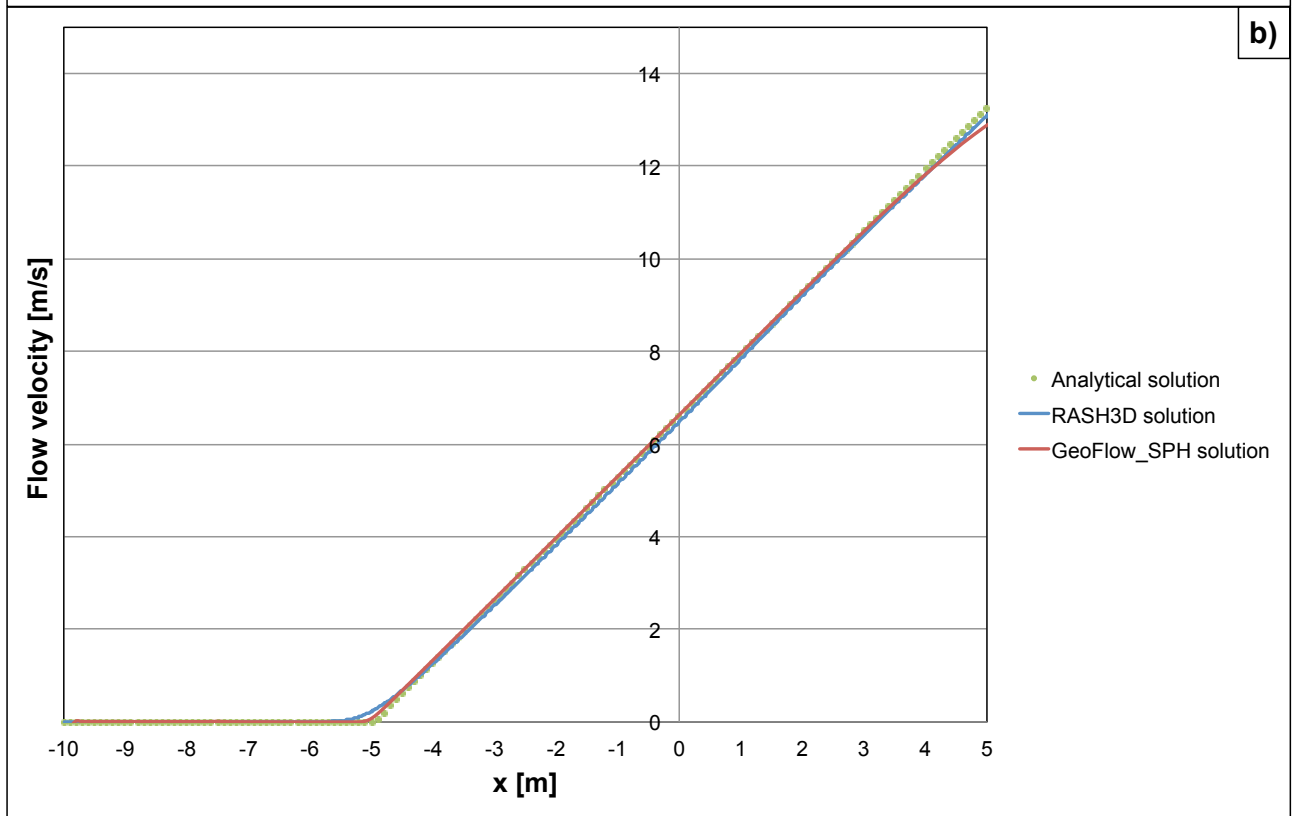
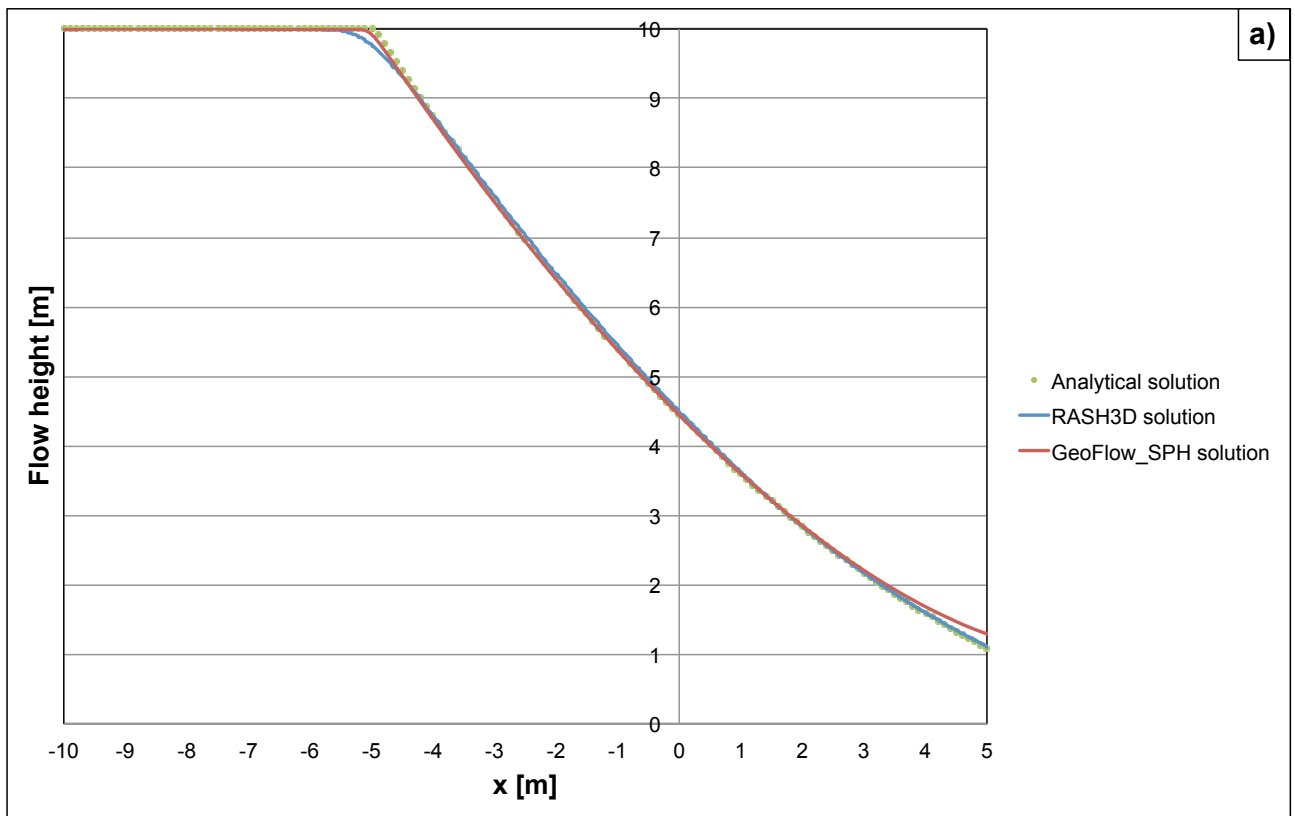
756



757

758 **Figure 3.** 1D dam break problem over a dry bed.

759

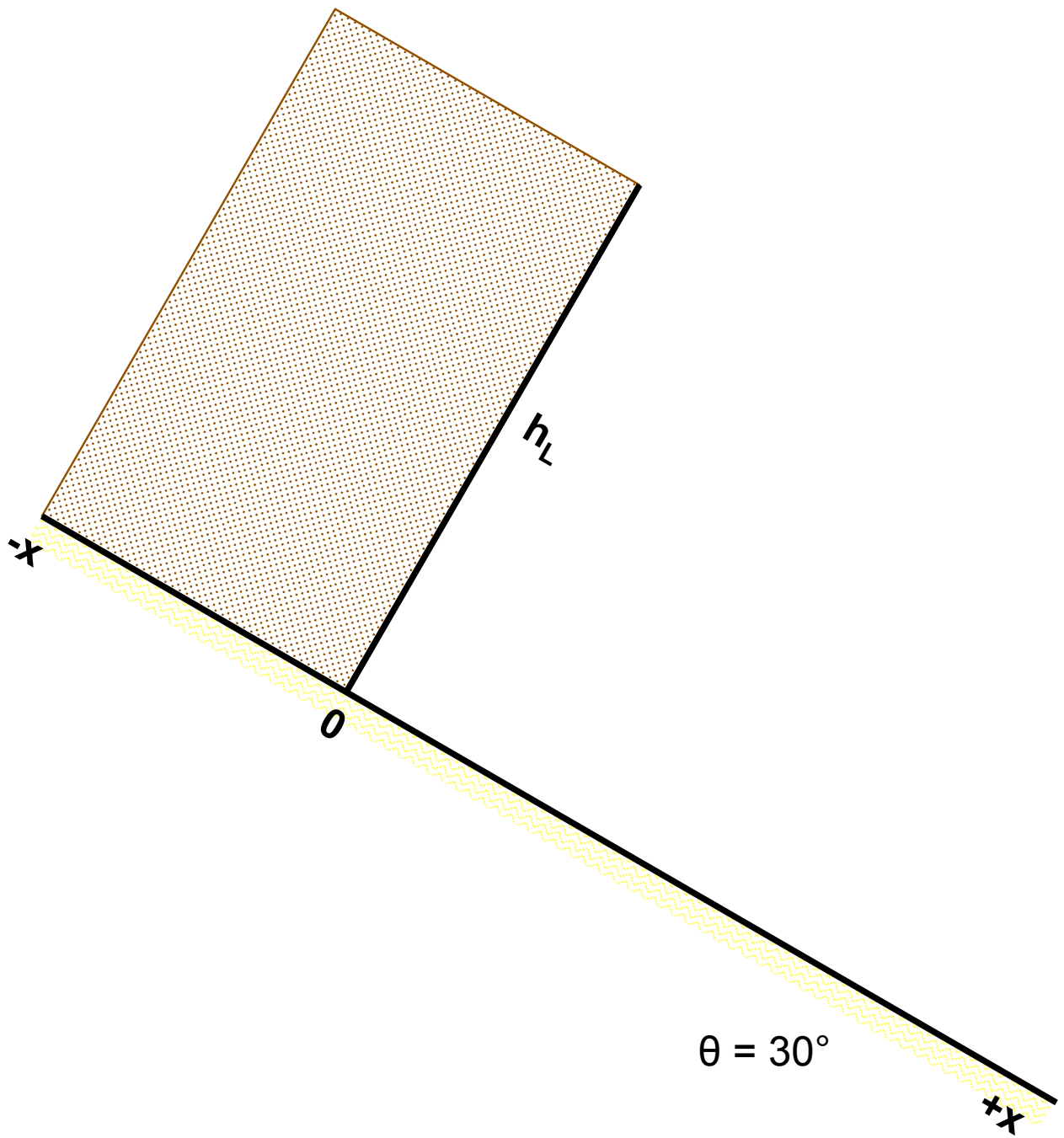


760

761 **Figure 4.** Comparison between analytical solution and computed results for flow height

762 (a) and velocity (b) at  $t = 0.5$  s.

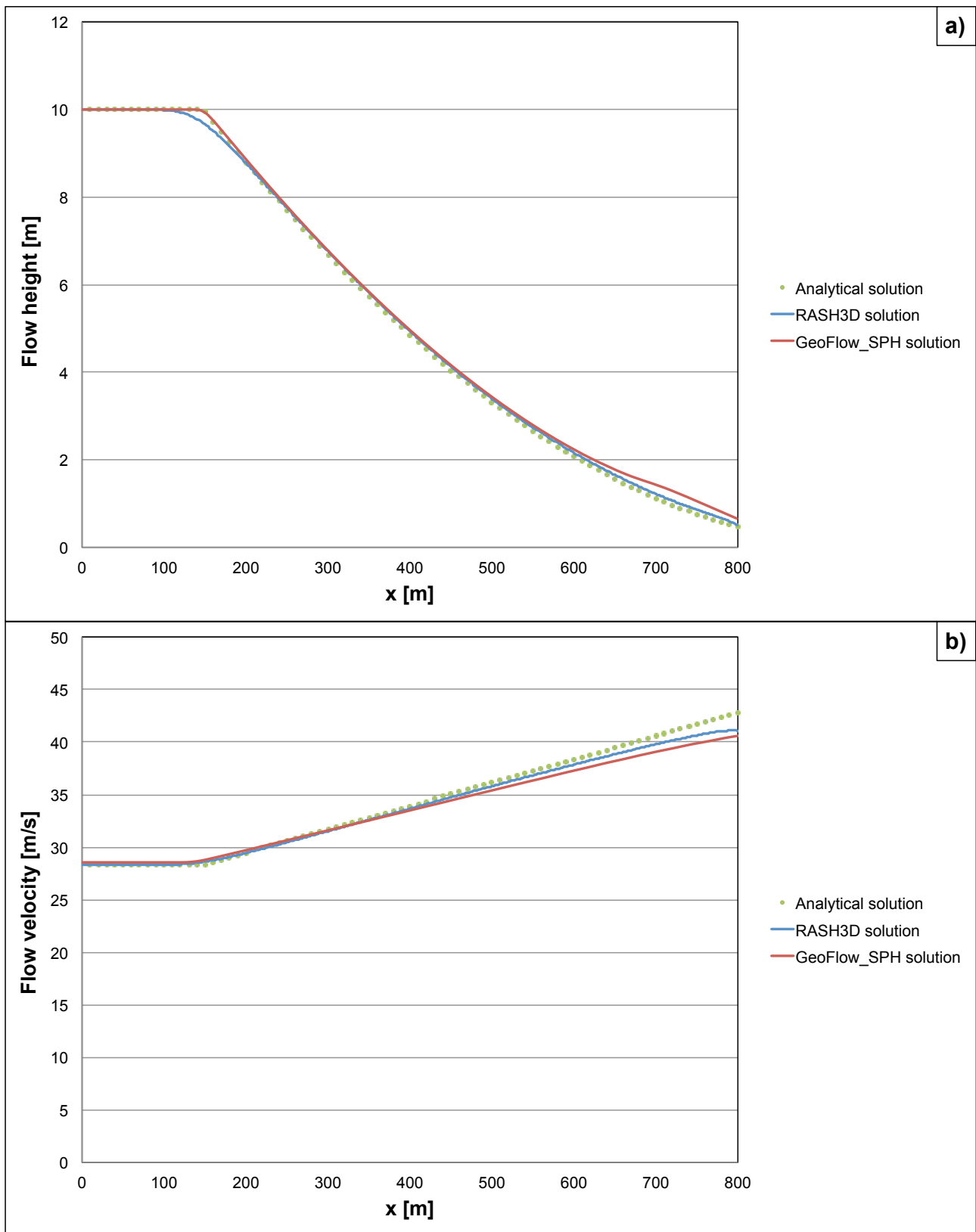
763



764

765 **Figure 5.** The frictional dam break problem on an inclined plane.

766

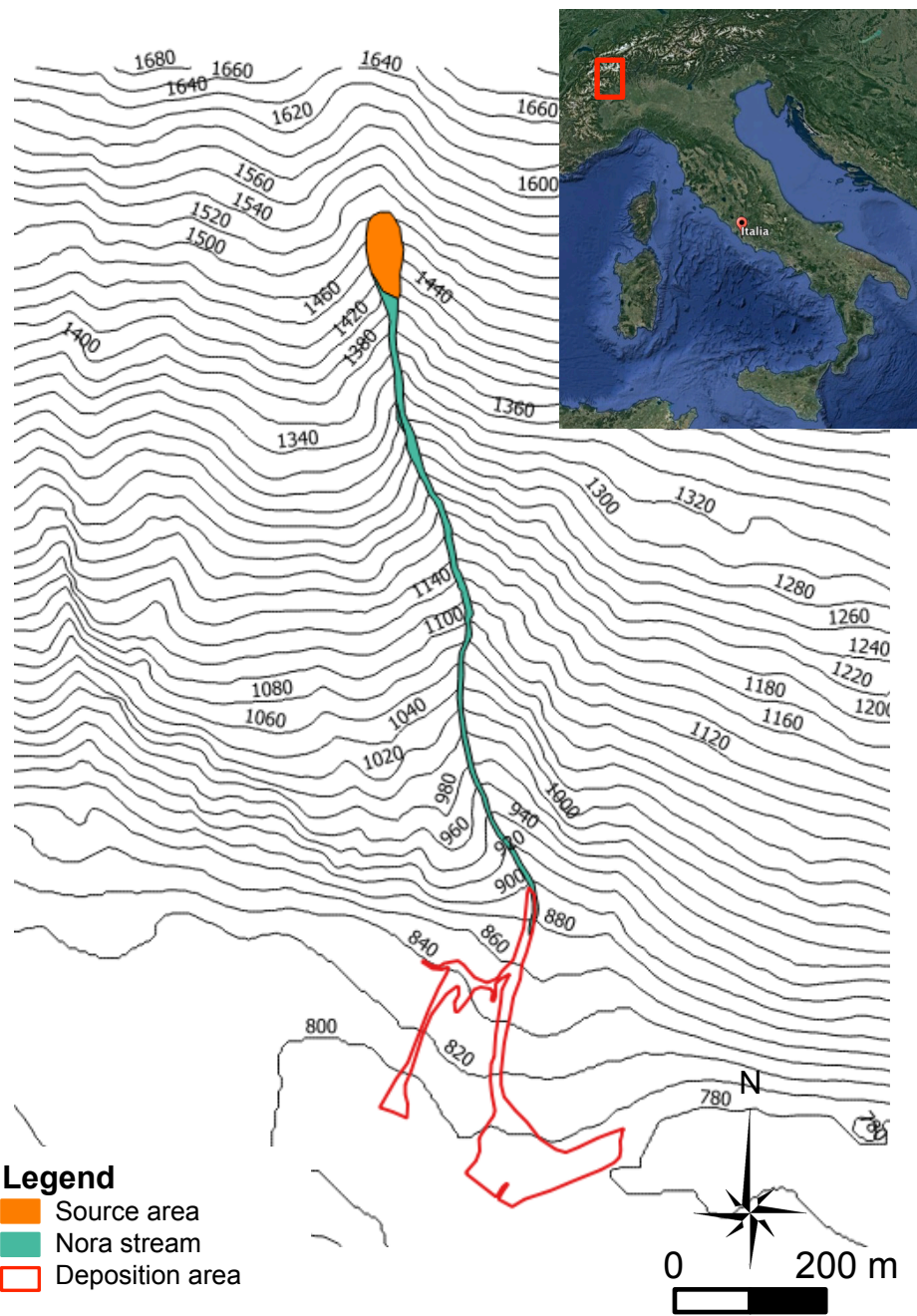


767

768 **Figure 6.** Comparison between analytical solution and computed results for flow height

769 (a) and velocity (b) at  $t = 30$  s.

770



771

772 **Figure 7.** Location of the Nora basin (Orco River valley) in Italy.

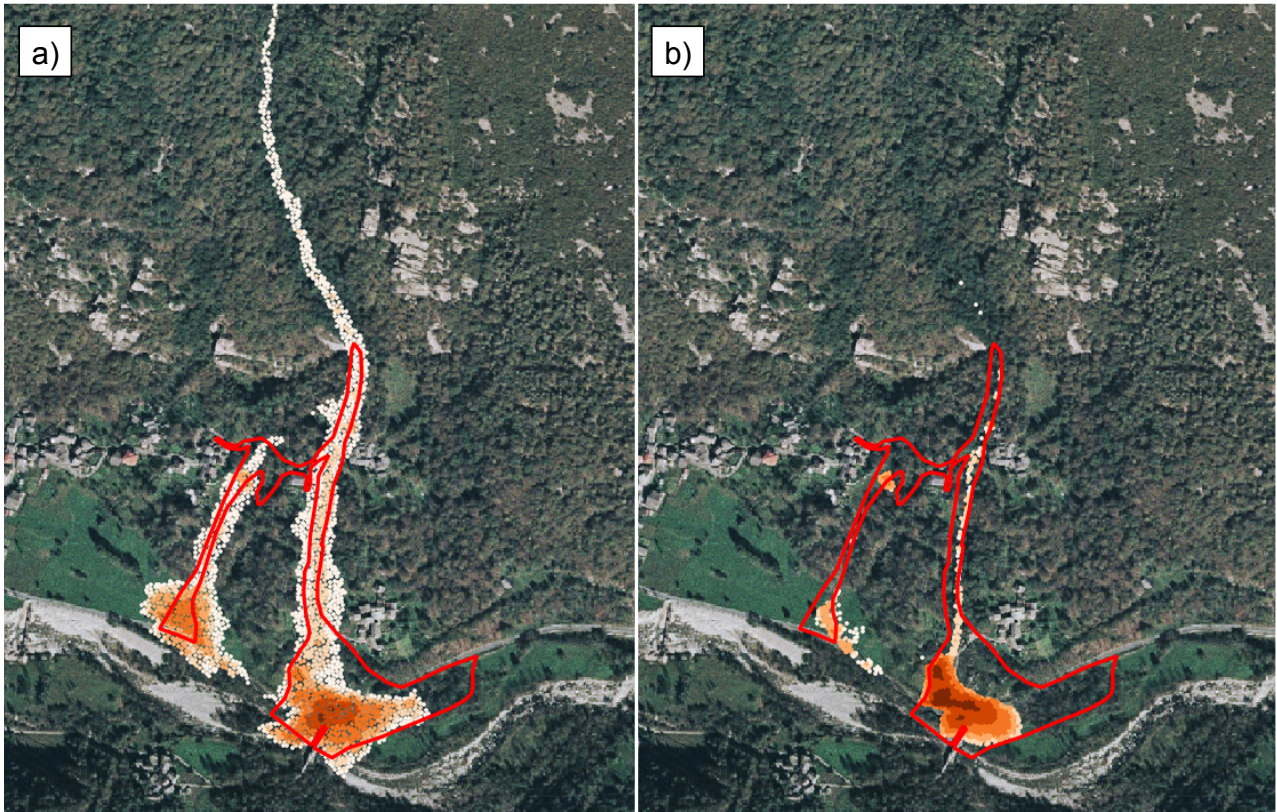
773



774

775 **Figure 8.** Deposition area and debris thickness distribution of the October 2000 Nora  
776 debris flow.

777



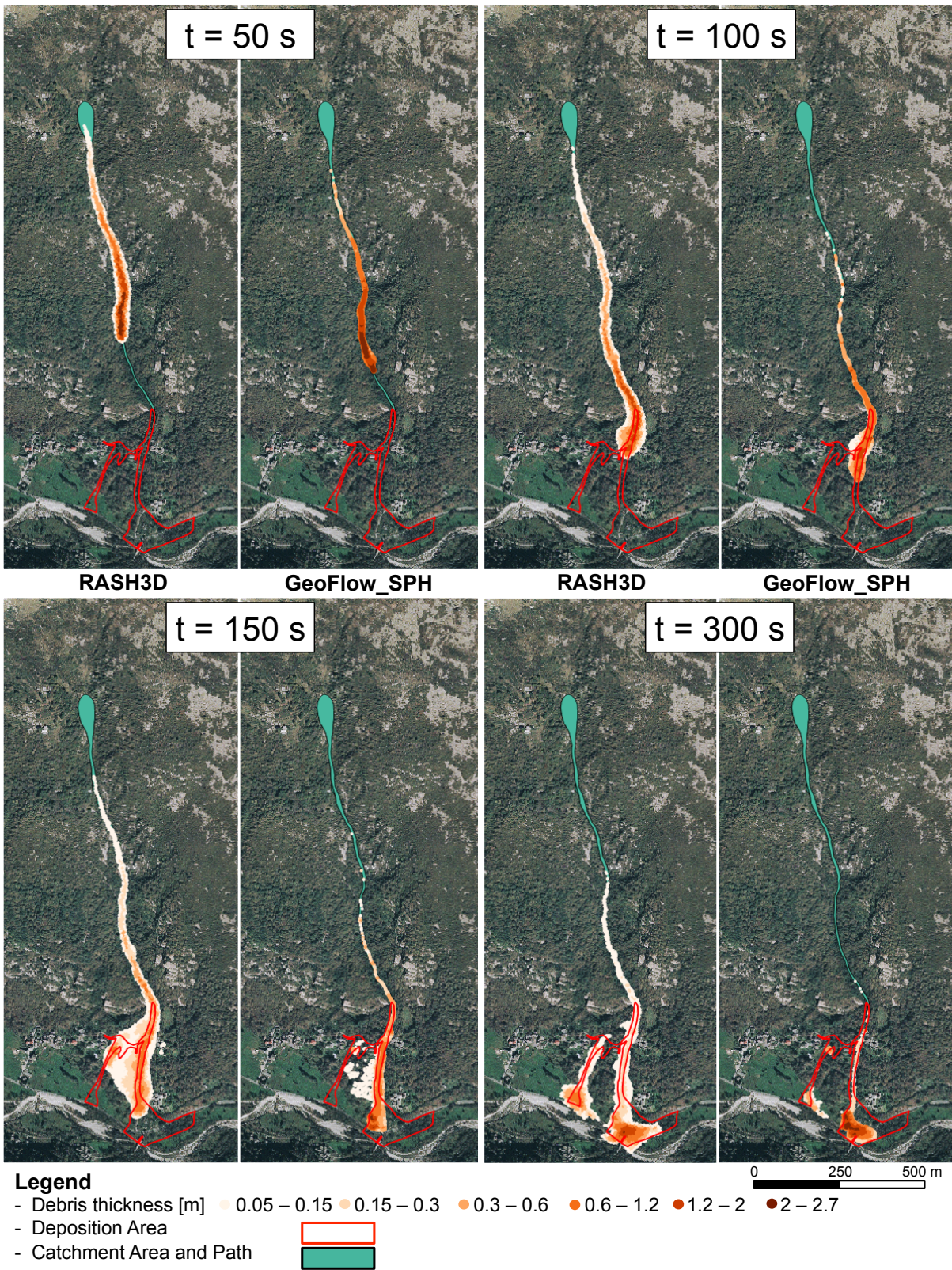
**Legend**

- Debris thickness [m]    ● 0.05 – 0.15   ● 0.15 – 0.3   ● 0.3 – 0.6   ● 0.6 – 1.2   ● 1.2 – 2   ● 2 – 2.7
- Deposition Area        □

778

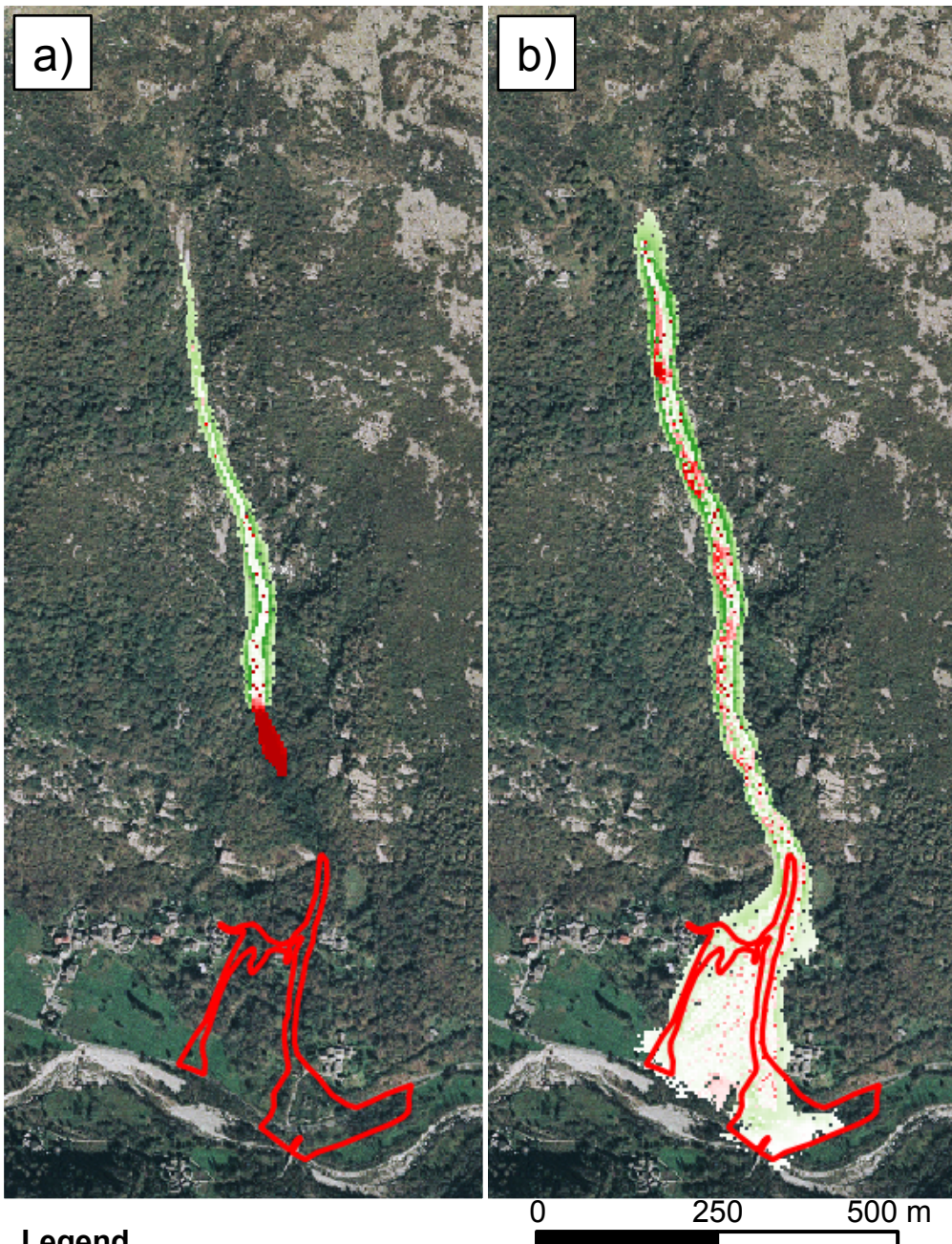
779 **Figure 9.** Comparison between RASH (a) and GeoFlow\_SPH (b) propagation path  
 780 (deposition values) at the end of the numerical simulation carried out using Voellmy  
 781 rheology with  $\mu=0,1$  and  $\xi=200 \text{ m/s}^2$ .

782



783

784 **Figure 10.** RASH3D (left) and GeoFlow\_SPH (right) simulation at different time steps  
 785 using the same rheological parameters. The two simulations show differences both in term  
 786 of velocity (flow simulated using SPH is faster) and shape (RASH3D shows a larger  
 787 lateral spreading).



**Legend**

- Velocity difference [m/s]    ■ -10   ■ -5   □ 0   ■ 5   ■ 10
- Deposition Area

788

789 **Figure 11.** Comparison of the two numerical code results in terms of velocity differences

790 at time step equal to 50 s (a) and velocity values obtained during whole simulation (b).



**Legend**

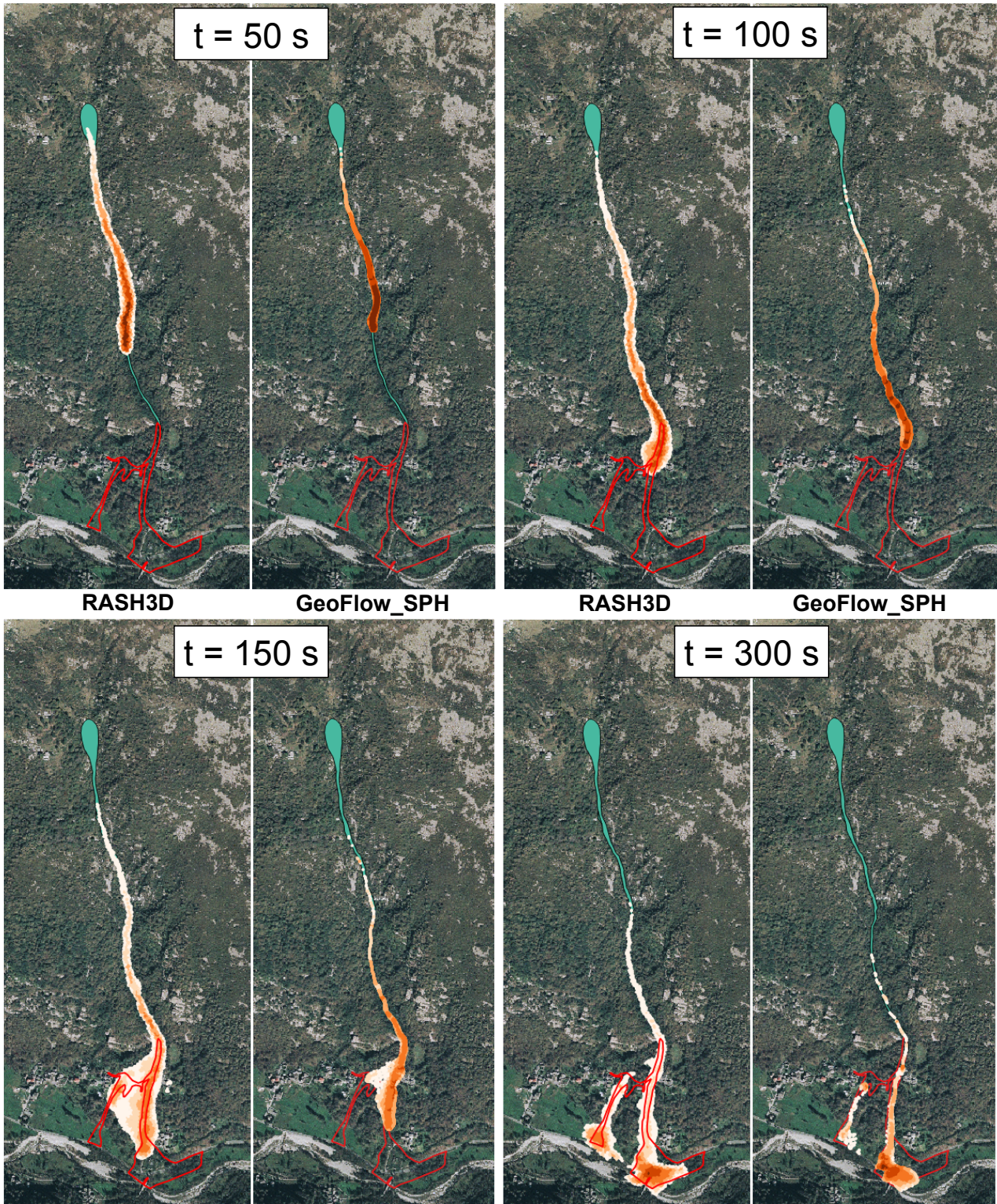
- Debris thickness [m]    ● 0.05 – 0.15   ● 0.15 – 0.3   ● 0.3 – 0.6   ● 0.6 – 1.2   ● 1.2 – 2   ● 2 – 2.7
- Deposition Area
- Catchment Area and Path

791

792 **Figure 12.** Back calculated GeoFlow\_SPH final deposit using Voellmy rheology with

793  $\mu=0,08$  and  $\xi=100 \text{ m/s}^2$ .

794



**Legend**

- Debris thickness [m]    0.05 – 0.15    0.15 – 0.3    0.3 – 0.6    0.6 – 1.2    1.2 – 2    2 – 2.7
- Deposition Area
- Catchment Area and Path

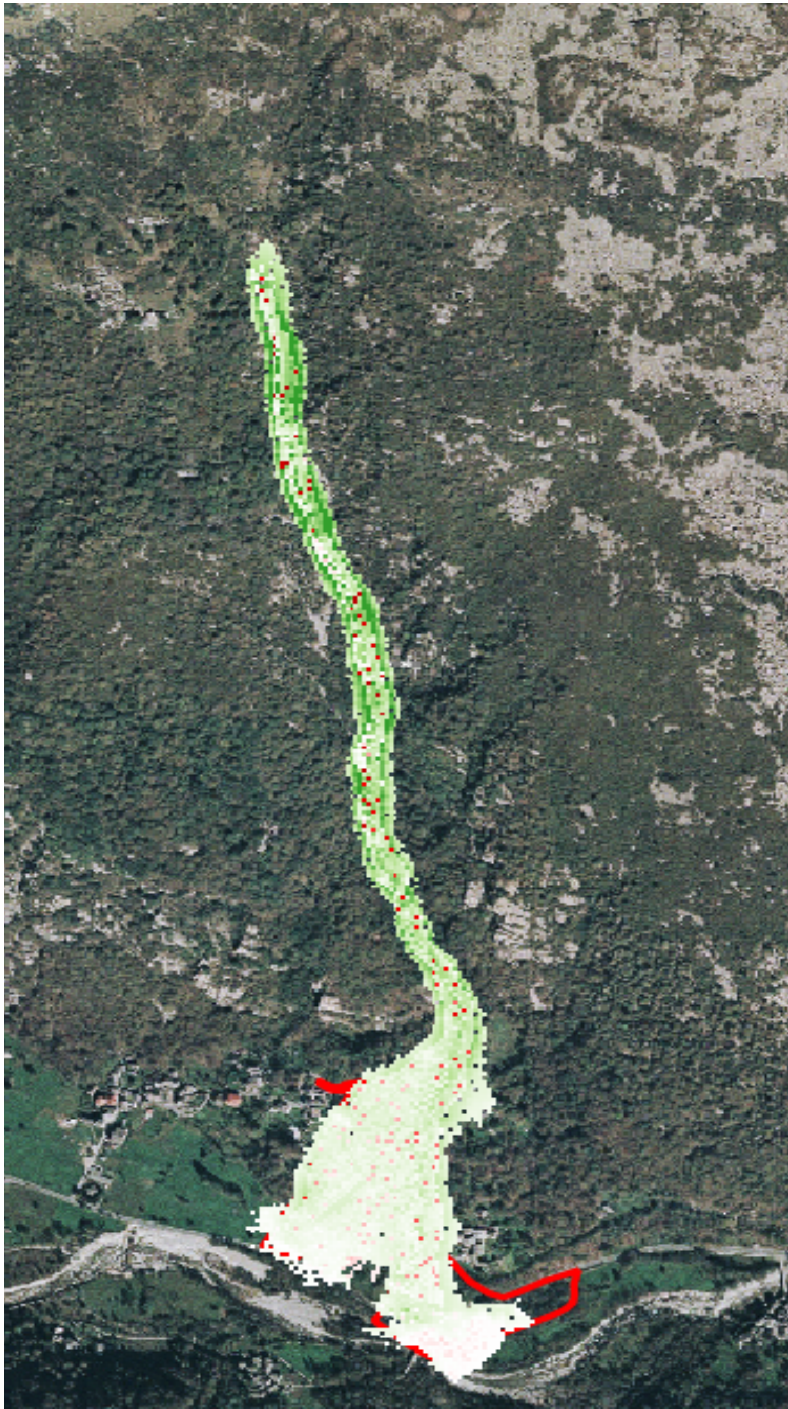
795

796

797

798

**Figure 13.** Comparison between RASH3D (left) and GeoFlow\_SPH (right) simulation at different time steps using Voellmy rheology with  $\mu=0,1$  and  $\xi=200 \text{ m/s}^2$  and  $\mu=0,08$  and  $\xi=100 \text{ m/s}^2$  respectively.



**Legend**

- Velocity difference [m/s]    ■ -10   ■ -5   □ 0   ■ 5   ■ 10
- Deposition Area

799

800 **Figure 14.** Differences between maximum velocity values evaluated during the whole  
 801 simulation using Geoflow\_SPH and RASH3D best-fit rheological parameters.

802